

## Article

# Periodic Signal Suppression in Position Domain Based on Repetitive Control

Haitao Li <sup>1,2,†</sup> , Xiangwen Chen <sup>1,2</sup> , Biao Xiang <sup>3,\*</sup>  and Xiaoyu Wang <sup>1,2,†</sup>

<sup>1</sup> School of Instrumentation Science and Optoelectronics Engineering, Beihang University (BUAA), Beijing 100191, China

<sup>2</sup> Ningbo Institute of Technology, Beihang University (BUAA), Ningbo 315800, China

<sup>3</sup> School of Mechano-Electronic Engineering, Xidian University, Xi'an 710071, China

\* Correspondence: xiangbiao@xidian.edu.cn

† The author contributed equally to this work.

**Abstract:** In this paper, a periodic signal suppression method in position domain based on repetitive control (RC) is proposed to realize high-precision speed control for the gimbal servo system of the single gimbal control moment gyro (SGCMG). To reduce the volume and weight while outputting large torque, the gimbal servo system usually needs to install the harmonic drive. However, the nonlinear transmission characteristics of the harmonic drive are also introduced into the gimbal servo system and make the speed fluctuate. Considering the speed fluctuation signal shown as a fixed frequency in the position domain, a position domain RC method combined with acceleration feedback is designed to realize the speed fluctuation minimization. The position domain RC improves the dynamic characteristics, while the acceleration feedback increases the damping of the system. To analyze the stability, the position domain RC is converted into the time domain through the domain transformation method, and a phase compensator is designed to improve the stability and increase the bandwidth of the position domain RC by compensating for the phase lag of the middle and low frequency, respectively. The feasibility and effectiveness of the proposed method are verified by the simulation and experimental results. These results illustrate that after applying the proposed approach, the output speed fluctuation and harmonic components decrease more than 20% and 24.1%, respectively.

**Keywords:** position domain RC; domain transformation; SGCMG; gimbal servo system; harmonic drive; harmonic analysis



**Citation:** Li, H.; Chen, X.; Xiang, B.; Wang, X. Periodic Signal Suppression in Position Domain Based on Repetitive Control. *Electronics* **2022**, *11*, 4069. <https://doi.org/10.3390/electronics11244069>

Academic Editor: Anna Richelli

Received: 2 November 2022

Accepted: 5 December 2022

Published: 7 December 2022

**Publisher's Note:** MDPI stays neutral with regard to jurisdictional claims in published maps and institutional affiliations.



**Copyright:** © 2022 by the authors. Licensee MDPI, Basel, Switzerland. This article is an open access article distributed under the terms and conditions of the Creative Commons Attribution (CC BY) license (<https://creativecommons.org/licenses/by/4.0/>).

## 1. Introduction

The single gimbal control moment gyro (SGCMG) is the primary attitude control actuator of large spacecraft because of good dynamic performance, high control accuracy and large output torque [1,2]. As shown in Figure 1, SGCMG is mainly composed of the high-speed rotor system and a gimbal servo system. The output torque of the SGCMG is  $M = H \times \omega$ , where  $H$  is the angular momentum of the high-speed rotor, and  $\omega$  is the angular speed of the gimbal servo system [3,4]. When the high-speed rotor runs stably, the value of  $H$  remains constant, and the output torque accuracy of the SGCMG is dependent on the precision of the  $\omega$  [5,6].

To meet the weight and volume requirements of the gimbal servo system, a harmonic drive is adopted to amplify the output torque, which has the advantages of light weight, small size, high efficiency, large transmission ratio and simple structure [7,8]. As shown in Figure 1, the harmonic drive is a special flexible transmission mechanism, which is composed of a wave generator, a flexspline and a circular spline [9]. The motion conversion of the harmonic drive is achieved by the elastic deformation of the flex spline [10]. However, this special transmission structure leads to nonlinear characteristics, such as nonlinear friction, kinematic error and hysteresis [11]. Among these characteristics, the kinematic

error is the major factor that causes the unexpected speed fluctuation of the gimbal servo system [12,13]. However, for the complex disturbances, the traditional control method is difficult to achieve satisfactory control results [14–16]. To achieve high-precision output speed of the gimbal servo system, it is crucial to suppress the influence of kinematic error on the speed.

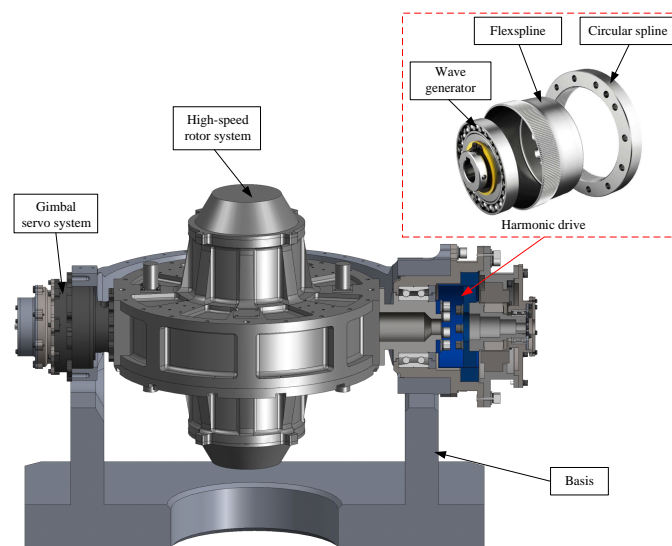


**Figure 1.** Structure diagram of SGCMG.

In recent decades, many researchers have studied the kinematic error of the harmonic drive. Kennedy et al. proposed that the kinematic error is mainly composed of the pure kinematic error caused by installing and manufacturing assembly and the torsion angle induced by the deformation of the flexspline [17]. Jia et al. illustrated that the tooth error is the major factor causing the pure kinematic error through the theoretical analysis [18]. To optimize the design of the conjugate contour teeth, the pure kinematic is analyzed in [19], and the effects of the load torque on the kinematic characteristics of the meshed teeth pairs is analyzed in [20]. Moreover, the function of the kinematic error with respect to angular position of the motor rotor was presented in [18]. Zhu et al. adopted the adaptive joint torque control method to improve the tracking accuracy of the angular position [21]. However, the algorithm requires the installation of torque sensors, and it is difficult to install additional torque sensors in the universal joint servo system due to the stringent design requirements. In [22], the kinematic error is converted into a state of the system by means of the Lagrange equation, and then it is observed by ESO. Liu et al. applied the double speed loops control method to suppress the speed fluctuation of the low speed servo system caused by the harmonic drive [23]. In [24], Tonshoff et al. proposed a nonlinear proportional-derivative (PD) control algorithm for closed-loop compensation of kinematic error, and the stability of the designed controller was proved by a Lyapunov function. Based on this method, the load angle position error could be close to zero.

Aiming at the periodicity of kinematic error, the iterative learning control [25] and repetitive control (RC) [26] have been applied to suppress the speed fluctuation. To suppress the vibration caused by kinematic error, a disturbance observer and a robust speed controller based on coprime decomposition were designed in [27]. Ma et al. adopted the method of adaptive joint torque to actively and adaptively track, but this method has high requirements for the detection device, and there may be hysteresis [28]. Li et al. applied the PD-type RC to suppress motion errors and proved the stability of the system through Lyapunov function [29]. These methods can generate infinity gain at the fundamental and multiplier frequency of the system to suppress or track periodic signals [30,31]. For linear continuous time invariant systems, a low-pass filter can be added after the RC to achieve high-precision tracking performance and nice suppression performance of the

disturbance [32]. However, Djouda et al. pointed out that when the harmonic frequency gradually increases, the low-pass filter will make the amplitude attenuation and phase lag of the system appear, which will affect the control accuracy of RC to suppress disturbance [33]. Ivan Godler et al. applied the composite control method to reduce the disturbance in a uniform velocity system, which combined the acceleration feedback and RC [12]. However, this method needs to be iterated again when the reference changes. Therefore, it is not suitable for a variable speed system, such as the gimbal servo system. To increase the bandwidth of the system and improve the performance of disturbance rejection, a phase compensator was designed in [34]. Nevertheless, the traditional plug-in RC cannot achieve better performance when the reference is time-varying. To solve this problem, some researchers applied the adaptive control into RC, and the internal model of RC could be adjusted with the change of disturbance period [35,36].

The speed fluctuation caused by the kinematic error is position period, and its frequency is twice the frequency of a motor angular position. Considering the periodic characteristics of speed fluctuation, a novel composite control method combining the RC and the acceleration feedback is proposed in this paper. The RC is designed in the position domain based on the domain conversion [37]. By this method, even if the reference speed changes, the frequency of the speed fluctuation is still fixed, and the RC does not need to reconstruct the internal model. Therefore, the algorithm can converge very quickly. The acceleration feedback can increase the damping of the system and further reduce the speed fluctuation. For convenience of reading, the performance and features of the relevant typical methods and the proposed method are summarized in Table 1.

**Table 1.** Performance summary about kinematic error suppression methods.

Method Type	References	Performance and Features
Torque control	[21]	<ul style="list-style-type: none"> <li>· Nice reference tracking performance</li> <li>· Strong robustness</li> <li>· Need install additional torque sensor</li> </ul>
Traditional RC	[27–31]	<ul style="list-style-type: none"> <li>· Nice speed fluctuation suppression performance</li> <li>· Not relying on the model or parameters</li> <li>· Need iterate again when reference changes</li> </ul>
The proposed method		<ul style="list-style-type: none"> <li>· Low hardware complexity (only position sensor)</li> <li>· Great for disturbance with position periodic</li> <li>· Not need iterate again when reference changes</li> </ul>

The rest of this article is organized as follows. Section 2 discusses the dynamic modeling of the gimbal servo system with harmonic drive. The compound control method is presented in Section 3, which combines acceleration feedback with position domain RC. The effectiveness and superiority of this method are verified by the simulation and experimental results in Section 4. In Section 5, some important conclusions are summarized.

## 2. Analysis of The Gimbal Servo System with Harmonic Drive

The structure of the gimbal servo system of SGCMG is shown in Figure 2. It is mainly composed of the motor-side encoder, bearings, permanent magnet synchronous motor (PMSM), harmonic drive, high-speed rotor system and load-side resolver.

According to [38], the PMSM can be simplified as a DC motor, and the equivalent electrical circuit is shown in Figure 3.

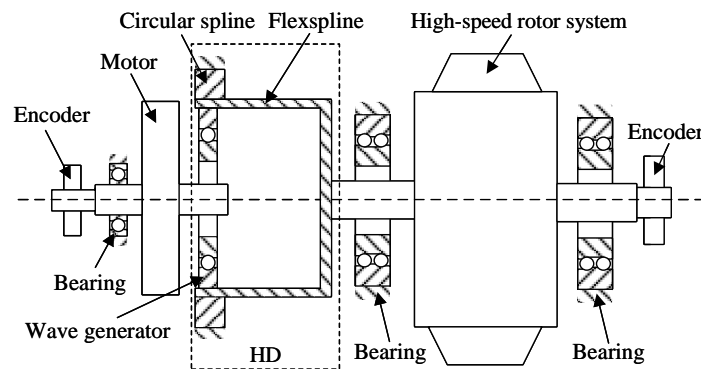


Figure 2. The structural schematic diagram of the gimbal servo system.

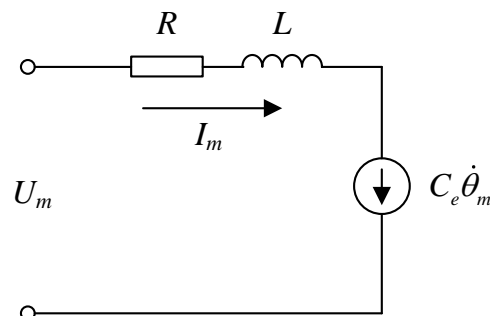


Figure 3. The equivalent electrical circuit of the DC motor.

On the basis of Figure 3, the balance equation of the voltage can be expressed as:

$$U_m = RI_m + L \frac{dI_m}{dt} + C_e \dot{\theta}_m \tag{1}$$

where  $U_m$  is the control voltage of the PMSM,  $T_m$  is the output torque of the PMSM,  $R$  is the stator phase resistance,  $I_m$  is the armature current,  $L$  is the phase inductance,  $C_e$  is the back electromotive force coefficient, and  $\theta_m$  is the angular position of the PMSM. The output torque  $T_m$  of the PMSM can be represented as:

$$T_m = K_m I_m \tag{2}$$

where  $K_m$  is the torque coefficient.

According to [38], the structure diagram of the gimbal servo system with harmonic drive is shown in Figure 4, and the dynamic model can be established as follows:

$$\begin{cases} T_l = K_e \Delta\theta \\ \omega_m = \dot{\theta}_m \\ \omega_l = \dot{\theta}_l \\ T_m = J_m \dot{\omega}_m + B_m \omega_m + T_l / N \\ T_l = J_l \dot{\omega}_l + B_l \omega_l + T_f \end{cases} \tag{3}$$

where  $T_l$  is the output torque of the harmonic drive,  $K_e$  is the torsional stiffness,  $\Delta\theta = \frac{\theta_m}{N} - \theta_l$  represents the torsional angle,  $\theta_l$  is the angular position of the load,  $\omega_m$  and  $\omega_l$  stand for the speed of the motor side and load side, respectively,  $J_m$  and  $J_l$  are the rotational inertia of the motor and load side, respectively,  $B_m$  and  $B_l$  represent the damping coefficient of the motor side and load side, respectively,  $T_f$  is other interference torque, and  $N$  is the ideal gear ratio of the harmonic drive.

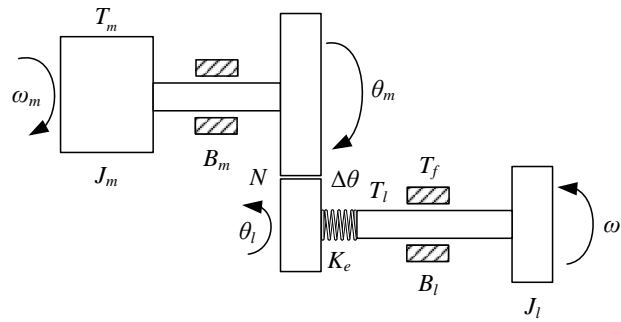


Figure 4. The structure diagram of the gimbal servo system.

To obtain the high-precision output speed of the gimbal servo system, double closed-loop feedback control methodology is applied in the gimbal servo system of SGCMG [38]. The inner is a current loop; the outer is a speed loop, and their loop controllers are all designed as a traditional PI controller which is described as  $G_i(s) = K_{pI} + \frac{K_I}{s}$  and  $G_v(s) = K_{pv} + \frac{K_v}{s}$ , respectively. The parameters of the  $G_i(s)$  and  $G_v(s)$  are shown in Table 2, which are calculated by the pole assignment method and fine-tuned by analyzing the Bode diagram.

Table 2. Parameters of the controller.

Parameter	Symbol	Value
Proportion of velocity loop	$K_{pv}$	0.29
Integral of velocity loop	$K_v$	2.25
Proportion of current loop	$K_{pI}$	001
Integral of current loop	$K_I$	0.01

Combining (1) and (3), the basic control block diagram of the gimbal servo system is shown in the Figure 5, where  $G_d(s) = \frac{1}{Ls+R}$ ,  $G_m(s) = \frac{1}{J_ms+B_m}$  and  $G_l(s) = \frac{1}{J_l s+B_l}$ .

From Figure 5, the load speed error caused by the kinematic error can be written as:

$$\omega_{er} = \frac{b_0 + b_1 + b_2}{a_0 + a_1 + a_2 + a_3} \theta_e \tag{4}$$

where

$$\begin{cases} b_0 = N^2 K_e s G_l(s) \\ b_1 = N^2 K_m K_e C_e s G_d(s) G_m(s) G_l(s) \\ b_2 = N^2 K_e s G_i(s) G_d(s) G_l(s) \\ a_0 = [G_v(s) G_i(s) + C_e] N^2 K_m K_e G_d(s) G_m(s) G_l(s) \\ a_1 = [N^2 K_m C_e s + K_e G_i(s)] G_d(s) G_m(s) \\ a_2 = [s + K_e G_l(s)] N^2 G_i(s) G_d(s) \\ a_3 = N^2 K_e G_l(s) + K_e G_m(s) + N^2 s \end{cases}$$

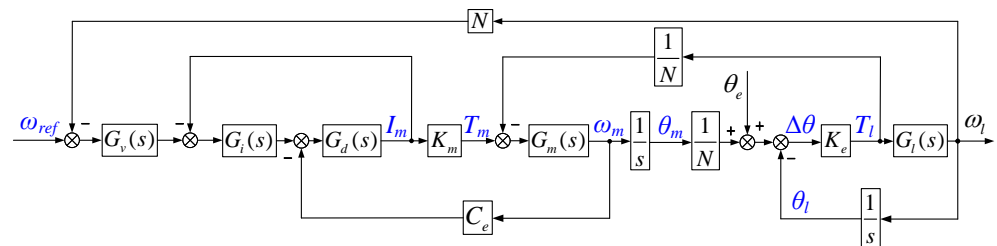


Figure 5. The block diagram of the gimbal servo control system.

According to [39], the model of the kinematic error can be described as:

$$\theta_e = A_1 \sin(2\theta_m) + A_2 \sin(4\theta_m) + A_3 \sin(6\theta_m) + \dots \tag{5}$$

where  $A_i$  ( $i = 1, 2, 3, \dots$ ) is the magnitude which is related to the speed of the motor and the load torque.

From (5), it can be seen that the kinematic error is related to the frequency of the motor's angular position, which has a fixed frequency in the position domain. The frequency is defined as:

$$\hat{f} = \frac{1}{\omega_m T} = \frac{1}{\omega_m} f \tag{6}$$

where  $f$  is the frequency with period  $T$  in the time domain, and  $\hat{f}$  is the frequency in the position domain.

The FFT analysis of the different speed conditions in the position domain are shown in Figure 6. It can be seen from Figure 6 that the speed fluctuation at different speeds has obvious constant frequency characteristics in the position domain. The main components are first-harmonic  $\hat{f}_1$ , second-harmonic  $\hat{f}_2$  and third-harmonic  $\hat{f}_3$ , and the other order harmonic content is relatively small. Therefore, we designed the position RC to suppress the three main order harmonics of the speed fluctuation.

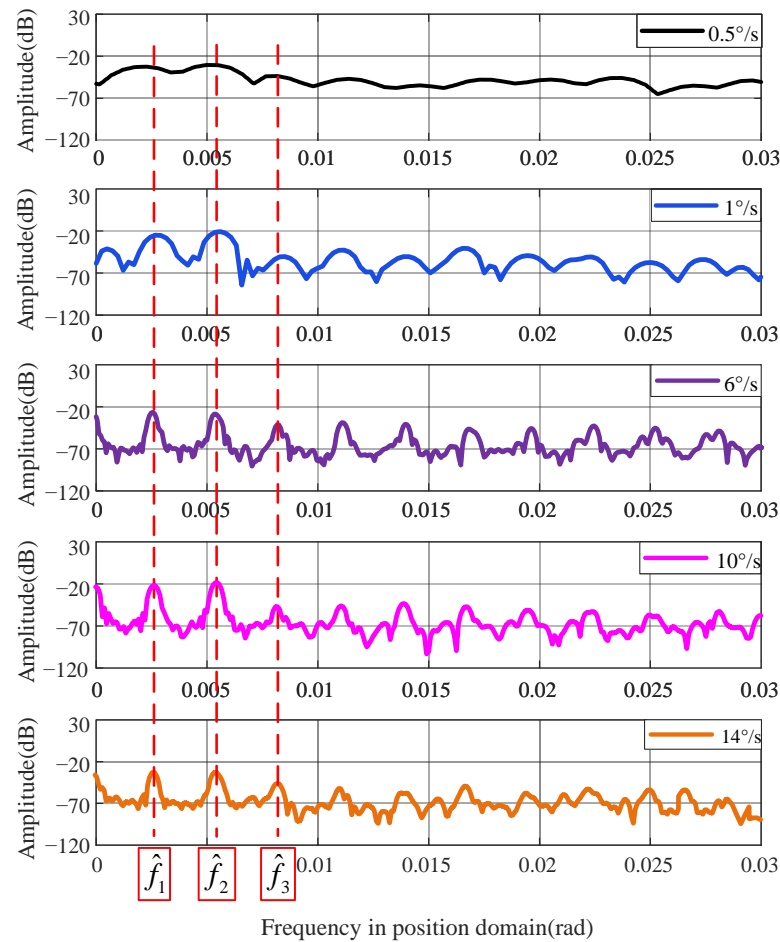


Figure 6. The position domain spectrogram of kinematic error.

### 3. Compound Control Scheme

#### 3.1. Design of Compound Controller

In order to suppress the speed fluctuation whose period is  $\lambda = 1/\hat{f}$ , the position domain plug-in RC system is introduced into the traditional double closed-loop controller. Then, it is mapped to the time domain through the principle of domain conversion and

realized by using the time sampling method. The position domain plug-in RC can be expressed as:

$$G_{rc}(\tilde{s}) = \frac{k_{rc}Q(s)e^{-\lambda\tilde{s}}}{1 - Q(s)e^{-\lambda\tilde{s}}}C(s) \quad (7)$$

where  $\tilde{s}$  is the Laplacian in the position domain,  $k_{rc}$  is the gain coefficient,  $Q(s)$  is the transfer function of the low-pass filter with the cut-off frequency  $\omega_c$ , which is designed to guarantee the stability and robustness of the system,  $e^{-\lambda\tilde{s}}$  is the delay element,  $\lambda$  is the position period of the speed fluctuation caused by the kinematic error of the harmonic drive, and  $C(s)$  is applied to ensure unity gain and zero phase in the middle- and low-frequency bands to improve the stability and dynamic performance of the system.

Let time  $t$  as the independent variable in the time domain and the angular position  $\theta_m$  be used as the independent variable in the position domain. The system object can be mapped in the time domain from the position domain by the domain conversion. This conversion method is an online conversion method based on an algorithm, similar to coordinate conversion, which is different from the conversion method based on the hardware mentioned in [40–43].

According to the domain conversion principle, when the variables are mapped between the time domain and the position domain, only the abscissa of the variables are mapped, and the physical nature of the variables are not changed. Then, the relationship of the signals between the time domain and position domain is described as:

$$x(t) = \hat{x}(\theta_m) \quad (8)$$

where  $x(t)$  is the state variable in the time domain, and  $\hat{x}(\theta_m)$  is the state variable in the position domain. The relationship between  $x(t)$  and  $\hat{x}(\theta_m)$  can be expressed as:

$$\frac{d\hat{x}(\theta_m)}{d\theta_m} = \frac{dt}{d\theta_m} \frac{d\hat{x}(\theta_m)}{dt} = \frac{1}{\omega_m(t)} \frac{dx(t)}{dt} \quad (9)$$

where  $\omega_m(t) = d\theta_m/dt$ .

According to (9), the relationship between  $\tilde{s}$  and  $s$  can be obtained.

$$\tilde{s} = \frac{1}{\omega_m(t)}s \quad (10)$$

Substituting (10) into (7), the RC can be reconstructed in the time domain.

$$G_{rc}(s) = \frac{k_{rc}Q(s)e^{-\frac{\lambda}{\omega_m(t)}s}}{1 - Q(s)e^{-\frac{\lambda}{\omega_m(t)}s}}C(s) \quad (11)$$

In order to increase the damping of the system [12], an acceleration feedback controller is added to the original speed loop.

$$G_a(s) = \frac{NB_I s}{K_e} \quad (12)$$

After combining the proposed composite control method, the overall block diagram of the gimbal servo control system is shown in Figure 7.



$$\begin{aligned}
 &|1 - k_{rc}C(\omega)G(\omega)(\cos(\varphi(\omega) + jk_{rc}\sin(\varphi(\omega)))| < 1 \\
 &\Rightarrow [1 - k_{rc}C(\omega)G(\omega)\cos(\varphi(\omega))]^2 + \\
 &[k_{rc}C(\omega)G(\omega)\sin(\varphi(\omega))]^2 < 1
 \end{aligned}
 \tag{19}$$

(19) can be simplified as:

$$k_{rc}C(\omega)G(\omega) < 2\cos(\varphi(\omega)) \tag{20}$$

Because  $k_{rc} > 0$ ,  $C(\omega) > 0$  and  $G(\omega) > 0$ , to satisfy (20),  $\varphi(\omega)$  should satisfy the following inequality.

$$-90^\circ < \varphi(\omega) < 90^\circ \tag{21}$$

The selection range of the gain coefficient,  $k_{rc}$  can be described as:

$$k_{rc} < \frac{\min[2\cos(\varphi(\omega))]}{\max[C(\omega)G(\omega)]} \tag{22}$$

### 3.3. Design of Phase Compensation

Refer to the parameter setting principle in [45]. The parameters of the PI are given in Table 3. The parameters of the gimbal servo system are also shown in Table 3.

**Table 3.** Parameters of the gimbal system based on an harmonic drive.

Parameter	Symbol	Value
Load moment of inertia	$J_l$	0.278 kg · m <sup>2</sup>
Load damping	$B_l$	0.8 N · m/(rad/s)
Motor moment of inertia	$J_m$	0.0011 kg · m <sup>2</sup>
Motor damping	$B_m$	0.02 N · m/(rad/s)
Torsional stiffness of harmonic drive	$K_e$	$3 \times 10^4$ N · m/rad
Torsional moment coefficient	$K_m$	0.65
Gear ratio	$N$	100
Inductance	$L$	0.01715 H
Stator phase resistor	$R$	3.2 Ω
Back EMF coefficient of motor	$C_e$	0.0562 V/(rad/s)
Gain coefficient of the RC	$k_{rc}$	1.4
Position period of $\hat{f}_1$	$\lambda_1$	180
Position period of $\hat{f}_2$	$\lambda_2$	90
Position period of $\hat{f}_3$	$\lambda_3$	45

The blue-dotted wave of Figure 8 shows the Bode plot of  $G(s)$ . It can be seen from Figure 8a that the original phase range of  $G(s)$  is  $\varphi(\omega) \in (-177^\circ, 122^\circ)$ , which does not satisfy (21). Therefore, a phase compensator  $C(s)$  needs to be appropriately designed.

$$C(s) = C_0(s)C_1(s)C_2(s) \tag{23}$$

where  $C_0(s)$  is the low-frequency compensator,  $C_1(s)$  stands for the middle-frequency compensator, and  $C_2(s)$  represents the high-frequency compensator.

According to the method of phase compensation method [26],  $C(s)$  can be designed as:

$$C(s) = \frac{0.1s + 1}{s} \cdot \frac{0.00666s + 1}{0.0029s + 1} \cdot \frac{0.00294s + 1}{0.0025s + 1} \tag{24}$$

It can be seen from the red wave of Figure 8a that  $\varphi(\omega) \in (-74^\circ, 70^\circ)$  satisfies the requirement of (21) in  $\omega \in (0, \omega_c)$  after phase compensation and  $\min|\cos\varphi(\omega)| = 0.275$ . Based on [46,47], from Figure 8b, it can be obtained that  $\max[C(\omega)G(\omega)] = -34$  dB = 0.02. According to (22), the gain coefficient range of control gain is  $0 < k_{rc} < 27.5$ .

In order to avoid the phase shift caused by the stable compensator  $Q(z)$ , based on [45], a zero-phase shift low-pass filter is designed as:

$$Q(z) = 0.25 + 0.5z^{-1} + 0.25z^{-2} \quad (25)$$

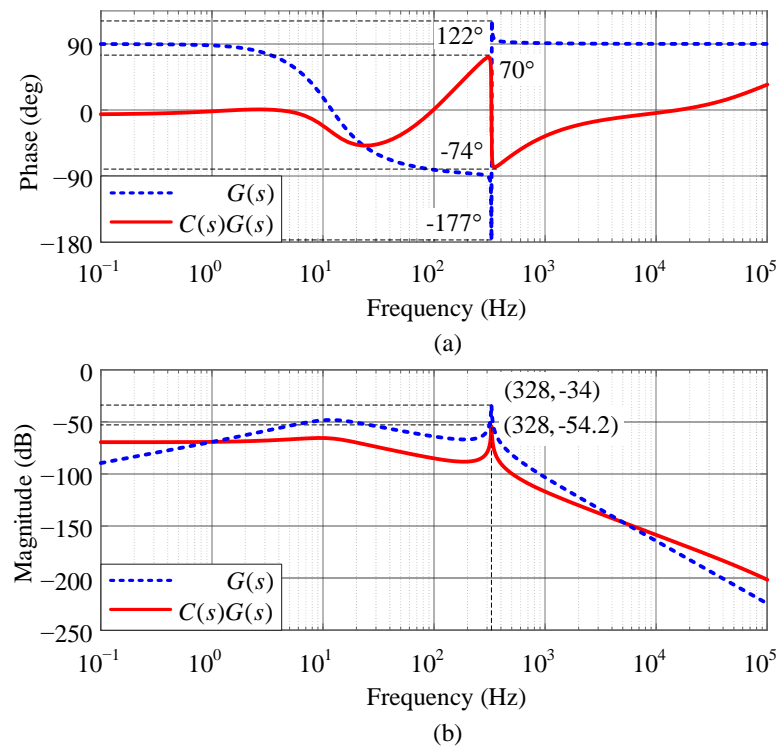


**Figure 8.** Frequency response curves: (a) phase response; (b) magnitude response.

## 4. Simulation and Experimental Verification

### 4.1. Experiment Setup

In order to verify the effectiveness of the proposed method, comparative experiments were conducted among three traditional control methods and the proposed method. Our experimental platform is shown in Figure 9, and the block diagrams of the experimental setup is shown in Figure 10. The gimbal servo system controller was composed of a digital signal processor (DSP) TMS320F28377 and field programmable gate array (FPGA) as the calculation module. TMS320F28377 had the advantages of low cost, low power consumption and high performance, which was applied to implement the algorithm and was also adopted to establish a PWM signal according to the control law output to drive the three-phase full bridge to generate the motor drive current. XC6SLX16 was used for signal processing of position sensor. The servo period of the control algorithm was 1 ms. The resolution of the angular position sensor was  $2\pi/2^{20}$  rad, the angular velocity range of the gimbal servo system was  $\pm 0.01^\circ/\text{s} - \pm 15^\circ/\text{s}$ , and the angular speed bandwidth of the gimbal servo system was 5 Hz.

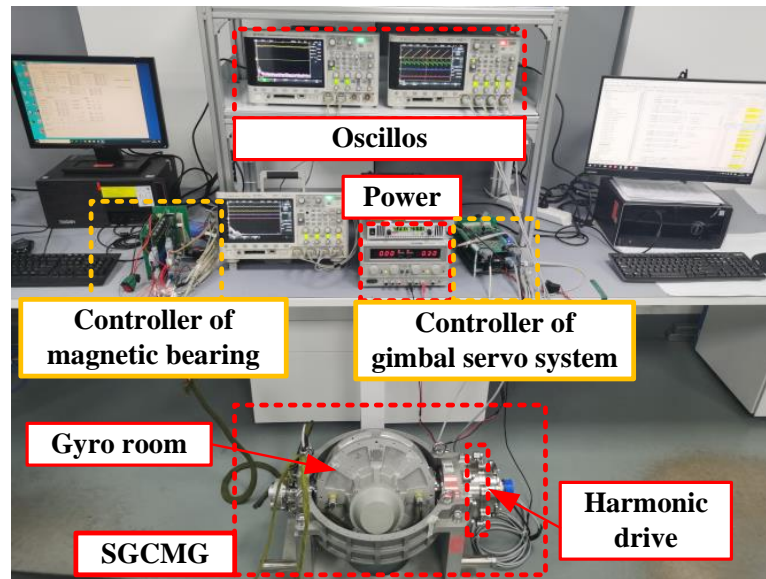


Figure 9. SGCMG prototype.

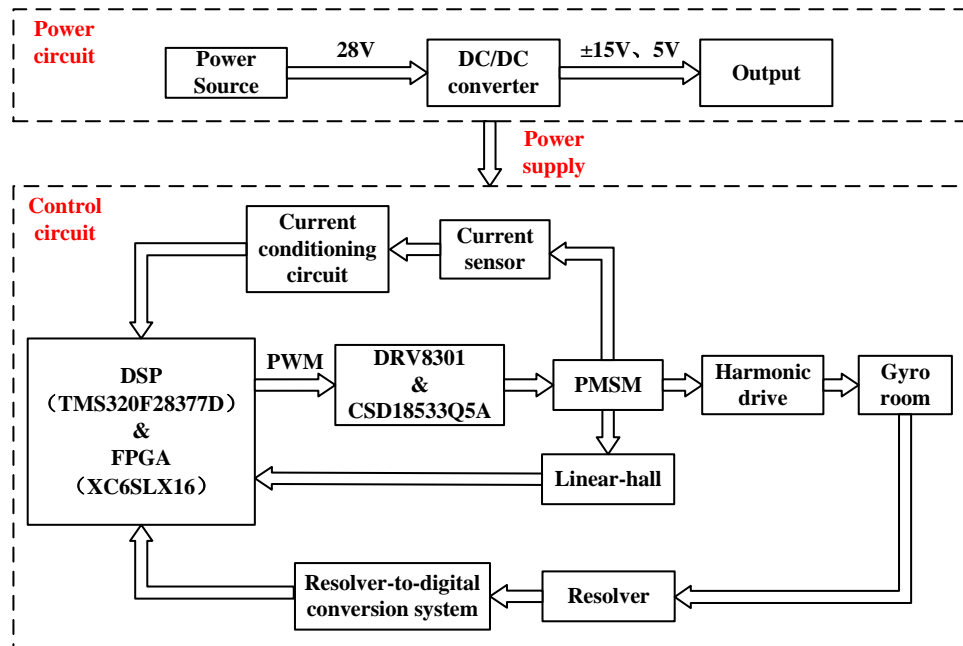


Figure 10. The block diagrams of the experimental setup.

#### 4.2. Simulation Verification

In order to verify the effectiveness of the proposed method, MATLAB/SIMULINK was used for simulation. For the position domain frequency of  $\hat{f}_1, \hat{f}_2, \hat{f}_3$ , the internal model of the position domain plug-in RC was designed as:

$$G_{rc1}(\tilde{s}) = \frac{Q(\tilde{s})e^{-180\tilde{s}}}{1 - Q(\tilde{s})e^{-180\tilde{s}}} \quad (26)$$

$$G_{rc2}(\tilde{s}) = \frac{Q(\tilde{s})e^{-90\tilde{s}}}{1 - Q(\tilde{s})e^{-90\tilde{s}}} \quad (27)$$

$$G_{rc3}(\tilde{s}) = \frac{Q(\tilde{s})e^{-45\tilde{s}}}{1 - Q(\tilde{s})e^{-45\tilde{s}}} \quad (28)$$

According to the analysis of the previous kinematic error as shown in (5) and the experimental data of our platform, its model can be regarded as:  $\theta_e = 0.002511 \sin(2\theta_m) + 0.001584 \sin(4\theta_m) + 0.00007943 \sin(6\theta_m)$ .

Figure 11 shows the comparison of different compound control methods. When the speed was set as  $6^\circ/\text{s}$ , it can be seen that the angular speed fluctuation with position domain RC decreased by 61.45% compared with traditional double closed-loop PI control and was reduced by 56.56% compared with the acceleration feedback. At the same time, the speed fluctuation was decreased by 20% compared with the plug-in RC. Table 4 compares the peak-to-peak values of the steady-state in Figure 11.

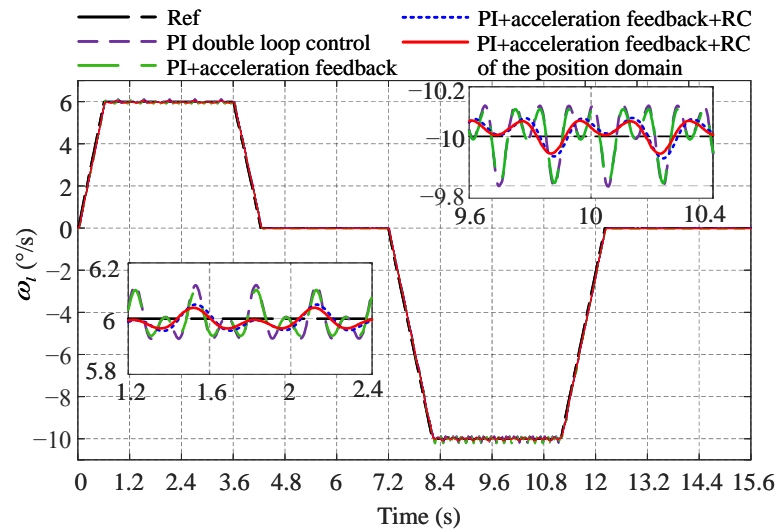


Figure 11. Simulation results of load angular speed curves at a steady speed motion.

Table 4. Peak-to-peak comparisons of steady state with different control methods.

Reference	PI	PI + Acceleration Feedback	PI + Acceleration Feedback + Plug-in RC	PI + Acceleration Feedback + Position Domain RC
$6^\circ/\text{s}$	$0.249^\circ/\text{s}$	$0.221^\circ/\text{s}$	$0.12^\circ/\text{s}$	$0.096^\circ/\text{s}$
$-10^\circ/\text{s}$	$0.431^\circ/\text{s}$	$0.425^\circ/\text{s}$	$0.211^\circ/\text{s}$	$0.177^\circ/\text{s}$

When the gimbal servo system moved in the reverse direction ( $-10^\circ/\text{s}$ ) compared with the traditional closed-loop PI control, the speed fluctuation was suppressed by 1.39% with the acceleration feedback method, 51.04% with the plug-in RC method and 58.93% with the position domain RC method.

In summary, the simulation results validate that the proposed method can effectively suppress the speed fluctuation caused by the kinematic error under steady state.

#### 4.3. Experimental Verification

To further validate the feasibility and effectiveness, comparative experiments between the traditional control methods and the proposed method were conducted. Due to the traditional plug-in RC not being suitable for the variable speed motion [35], the experiment of this method was not carried out.

With the reference speed of  $6^\circ/\text{s}$ , Figure 12 shows the steady-state speed curves corresponding to different control methods. The peak-to-peak speed error value of the PI double-loop control and the PI + acceleration feedback was about  $0.96^\circ/\text{s}$  and  $0.86^\circ/\text{s}$ , respectively. Compared with the two aforementioned methods, when the position domain RC method was introduced, the peak-to-peak value became only about  $0.44^\circ/\text{s}$  which was decreased about 54.17% and 48.83%, respectively. From the results, it can be seen that

the position domain RC method has the best speed fluctuation inhibition effect under the constant speed condition.

Figure 13 reveals the comparison results of the speed harmonic with the different control methods in the frequency domain. To be more intuitive, the speed harmonic comparison results are shown in Table 5. It can be seen from Table 5 that the speed fluctuation can be attenuated effectively with the proposed control method.

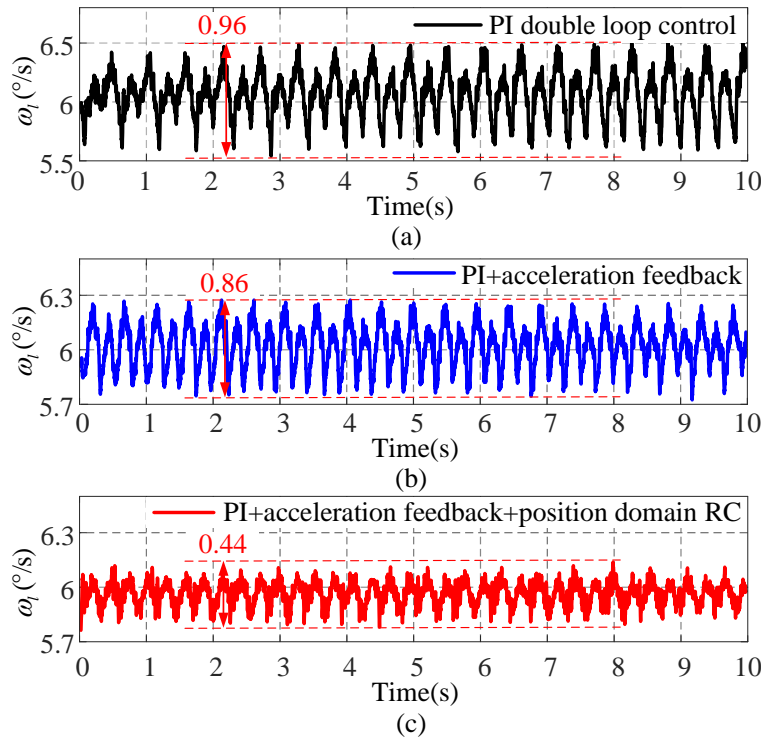


Figure 12. Experimental results of the steady-state response in time domain speed: (a) PI double loop control; (b) PI+acceleration feedback; (c) PI+acceleration feedback+position domain RC.

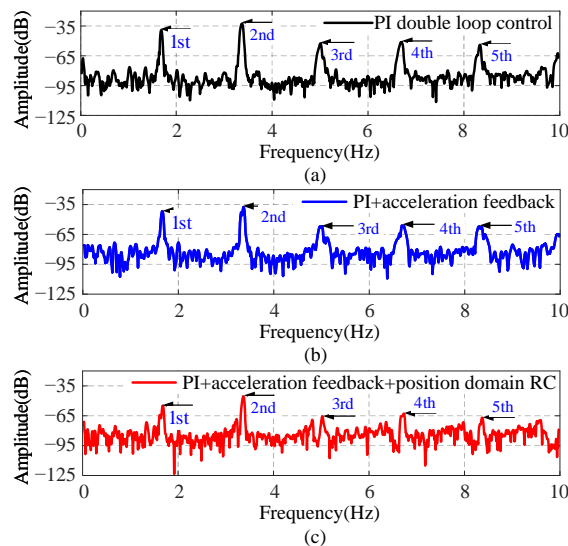
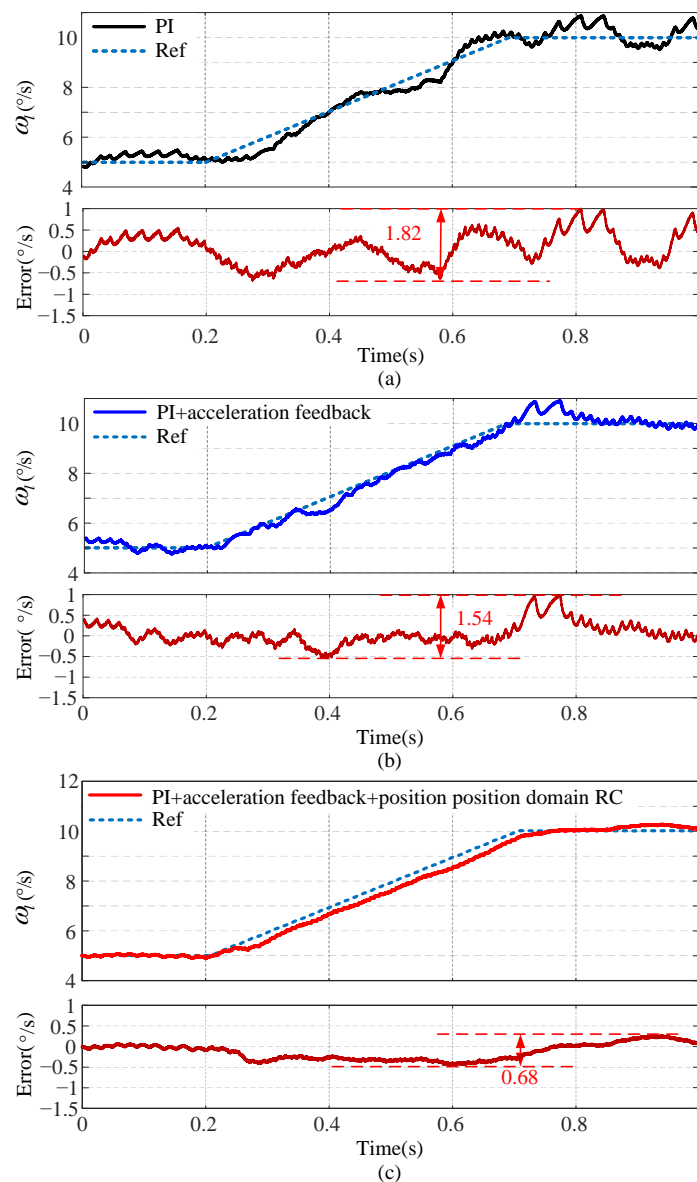


Figure 13. Experimental results of the steady-state response in frequency domain speed: (a) PI double loop control; (b) PI+acceleration feedback; (c) PI+acceleration feedback+position domain RC.

**Table 5.** Comparison results of speed harmonic with different control methods.

	1st	2nd	3rd	4th	5th
PI double-loop control	−39 dB	−33 dB	−52 dB	−51 dB	−54 dB
PI+Acceleration feedback	−43 dB	−35 dB	−57 dB	−54 dB	−58 dB
PI+Acceleration feedback+Position domain RC	−56 dB	−46 dB	−65 dB	−64 dB	−67 dB

The speed dynamic response comparison experiments were carried out with the different control methods. As shown in Figures 14 and 15, the reference values of load speed were  $5^\circ/\text{s}$  and  $10^\circ/\text{s}$ , respectively. At 0.2 s, the acceleration was given separately as  $10^\circ/\text{s}^2$  and  $-10^\circ/\text{s}^2$ . The values of load speed were individually turned to  $10^\circ/\text{s}$  and  $5^\circ/\text{s}$ .



**Figure 14.** Experimental results of load angular speed and tracking error at variable speed motion: (a) PI; (b) PI+acceleration feedback; (c) PI+acceleration feedback+position domain RC.

When the gimbal servo system turned forward, it can be seen from Figure 14 that the speed tracking error was  $0.68^\circ/\text{s}$ , which is the smallest compared with the other methods. When the gimbal servo system turned deceleration, the proposed method also had the best speed tracking effect. In Figure 15, it can be observed that the tracking error with

the proposed position domain RC was the smallest ( $0.58^\circ/s$ ). To obtain a more intuitive comparison effect, the speed fluctuation values under different methods are summarized in the Table 6.

**Table 6.** The peak-to-peak speed at variable speed motion.

Reference Acceleration	PI	PI + Acceleration Feedback	PI + Acceleration Feedback + Position Domain RC
$10^\circ/s^2$	$1.82^\circ/s$	$1.54^\circ/s$	$0.68^\circ/s$
$-10^\circ/s^2$	$1.76^\circ/s$	$1.23^\circ/s$	$0.58^\circ/s$

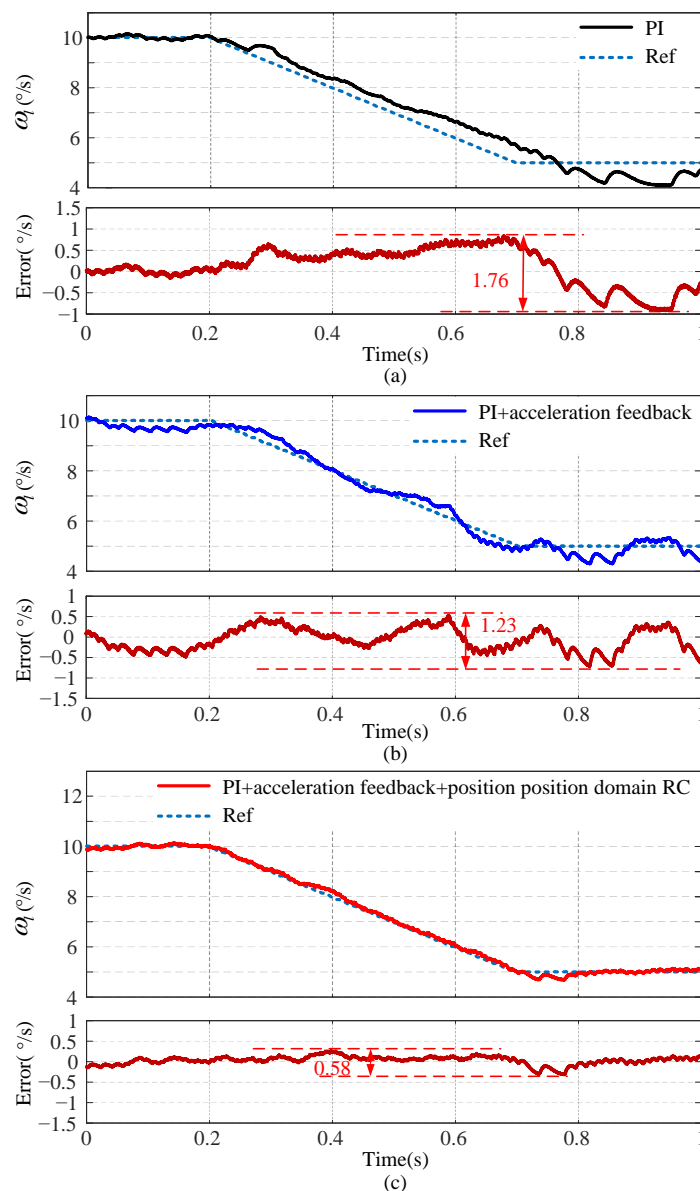


**Figure 15.** Experimental results of load angular speed and tracking error at reverse variable speed motion: (a) PI; (b) PI+acceleration feedback; (c) PI+acceleration feedback+position domain RC.

From the aforementioned experiments, it can be concluded that the control method proposed in this paper not only improves the steady-state suppression performance of the speed fluctuation, but also has the best dynamic response performance compared with

the other control methods. Consequently, the feasibility and effectiveness of the proposed method in this paper is demonstrated.

## 5. Conclusions

This paper proposes a compound control method to suppress speed fluctuation of the gimbal servo system equipped with a harmonic drive. At first, based on the establishment and analysis of the gimbal servo system model with a harmonic drive, a composite control method based on acceleration feedback and position domain RC was designed. Then, the phase compensator was designed to compensate for the phase lag of the position domain RC output, which improves the stability and the bandwidth of the system. Finally, simulations and experiments were carried out to verify that the proposed method can effectively suppress the speed fluctuation caused by the kinematic error. The experimental results illustrate that after applying the proposed approach, the output speed fluctuation and harmonic components decrease more than 20% and 24.1%, respectively. Eventually, because the disturbance is widespread in practical systems, the proposed method can be extended to other practical projects.

**Author Contributions:** Conceptualization, H.L. and X.C.; methodology, X.C. and X.W.; software, X.C.; validation, H.L.; formal analysis, B.X.; investigation, H.L., X.C. and X.W.; Data curation, X.C. and X.W.; writing—original draft, H.L., X.C., B.X. and X.W.; writing—review and editing, B.X.; supervision, H.L. and B.X. All authors have read and agreed to the published version of the manuscript.

**Funding:** This work was supported by the National Natural Science Foundation of China under Grant 62173015, 62122009 and 51925501.

**Institutional Review Board Statement:** This article does not contain any experiments with human or animal participants performed by any of the authors.

**Conflicts of Interest:** The authors declare that they have no conflict of interest.

## References

1. Li, H.; Wang, Y.; Han, B.; Chen, X. High-precision composite control based on dual-sampling-rate extended state observer for ultra-low speed gimbal servo system. *IEEE J. Emerg. Sel. Top. Power Electron.* **2022**, *10*, 5423–5434. [[CrossRef](#)]
2. Han, B.; Chen, Y.; Zheng, S.; Li, M.; Xie, J. Whirl mode suppression for AMB-rotor systems in control moment gyros considering significant gyroscopic effects. *IEEE Trans. Ind. Electron.* **2021**, *68*, 4249–4258. [[CrossRef](#)]
3. Zheng, S.; Li, H.; Han, B.; Yang, J. Power consumption reduction for magnetic bearing systems during torque output of control moment gyros. *IEEE Trans. Power Electron.* **2017**, *32*, 5752–5759. [[CrossRef](#)]
4. Li, H.; Chen, X.; Zhang, H.; Cui, X. High-precision speed control for low-speed gimbal systems using discrete sliding mode observer and controller. *IEEE J. Emerg. Sel. Top. Power Electron.* **2022**, *10*, 2871–2880. [[CrossRef](#)]
5. Li, H.; Zheng, S.; Ning, X. Precise control for gimbal system of double gimbal control moment gyro based on cascade extended state observer. *IEEE Trans. Ind. Electron.* **2017**, *64*, 4653–4661. [[CrossRef](#)]
6. Shi, Y.; Li, H.; Han, B. Position extraction of ultralow-speed gimbal servo system with linear hall sensors. *IEEE Trans. Ind. Electron.* **2022**, *69*, 2947–2955. [[CrossRef](#)]
7. Han, B.; Zheng, S.; Li, H.; Liu, Q. Weight-reduction design based on integrated radial-axial magnetic bearing of a large-scale MSCMG for space station application. *IEEE Trans. Ind. Electron.* **2017**, *64*, 2205–2214. [[CrossRef](#)]
8. Shi, Y.; Yu, Y.; Li, H.; Han, B.; Liu, X.; Chen, X. Speed fluctuation suppression by model-based feed-forward control in gimbal system with harmonic drive. *IEEE Trans. Power Electron.* **2022**, *37*, 6678–6687. [[CrossRef](#)]
9. Golder, I.; Hashimoto, M.; Horiuchi, M.; Ninomiya, T. Performance of gain-tuned harmonic drive torque sensor under load and speed conditions. *IEEE/ASME Trans. Mechatron.* **2001**, *6*, 155–160.
10. Zhang, H.; Ahmad, S.; Liu, G. Torque estimation for robotic joint with harmonic drive transmission based on position measurements. *IEEE Trans. Robot.* **2006**, *22*, 685–695. [[CrossRef](#)]
11. Li, H.; Ning, X.; Han, B. Speed tracking control for the gimbal system with harmonic drive. *Control Eng. Prac.* **2017**, *58*, 204–213. [[CrossRef](#)]
12. Godler, I.; Ohnishi, K.; Yamashita, T. Repetitive control to reduce speed ripple caused by strain wave gearing. In Proceedings of the IECON'94—20th Annual Conference of IEEE Industrial Electronics, Bologna, Italy, 5–9 September 1994; Volume 2, pp. 1034–1038.
13. Jung, B.J.; Kim, B.; Koo, J.C.; Choi, H.R.; Moon, H. Joint torque sensor embedded in harmonic drive using order tracking method for robotic application. *IEEE/ASME Trans. Mechatron.* **2017**, *22*, 1594–1599. [[CrossRef](#)]
14. Sahin, M.E.; Okumus, H.I. Comparison of different controllers and stability analysis for photovoltaic powered buck-boost DC-DC converter. *Electr. Power Components Syst.* **2018**, *46*, 149–161. [[CrossRef](#)]

15. Ekren, O.; Sahin, S.; Isler, Y. Comparison of different controllers for variable speed compressor and electronic expansion valve. *Int. J. Refrig.* **2010**, *33*, 1161–1168. [[CrossRef](#)]
16. Taher, S.A.; Hemmati, R.; Abdolalipour, A.; Akbari, S. Comparison of different robust control methods in design of decentralized UPFC controllers. *Int. J. Electr. Power Energy Syst.* **2012**, *43*, 173–184. [[CrossRef](#)]
17. Kennedy, C.W.; Desai, J.P. Modeling and control of the mitsubishi PA-10 robot arm harmonic drive system. *IEEE/ASME Trans. Mechatron.* **2005**, *10*, 263–274. [[CrossRef](#)]
18. Jia, H.; Li, J.; Xiang, G.; Wang, J.; Xiao, K.; Han, Y. Modeling and analysis of pure kinematic error in harmonic drive. *Mech. Mach. Theory* **2021**, *155*, 104122. [[CrossRef](#)]
19. Gravagno, F.; Mucino, V.H.; Pennestrì, E. Influence of wave generator profile on the pure kinematic error and centrodes of harmonic drive. *Mech. Mach. Theory* **2016**, *104*, 100–117. [[CrossRef](#)]
20. D. H. Ma, P. F. Rao, S.Z.Y.; Wang, Y. Kinematic analysis of meshed teeth pairs of harmonic drive gears considering the load effect using computer vision. In Proceedings of the 2019 5th International Conference on Control, Automation and Robotics (ICCAR), Beijing, China, 19–22 April 2019; pp. 212–217.
21. Zhu, W. Precision control of robots with harmonics drives. In Proceedings of the 2007 IEEE International Conference on Robotics and Automation, Roma, Italy, 10–14 April 2007; pp. 3831–3834.
22. Li, H.; Yang, S.; Kong, L.; Wen, T. High-precision angular speed tracking control of gimbal system with harmonic reducer. *IEEE Trans. Ind. Electron.* **2022**, *69*, 8168–8177. [[CrossRef](#)]
23. Liu, P.; Wu, Z. Resonance analysis and suppression of harmonic reducer in low speed servo system. In Proceedings of the 2018 Chinese Control And Decision Conference (CCDC), Shenyang, China, 9–11 June 2018; pp. 2873–2878.
24. Tonshoff, H.K.; Kummert, J. Active compensation of kinematic errors in servo drives for machine tools and robots. In Proceedings of the American Control Conference, San Diego, CA, USA, 2–4 June 1999; pp. 2590–2594.
25. Hao, S.; Liu, T.; Paszke, W. Robust iterative learning control for batch processes with input delay subject to time-varying uncertainties. *IET Control Theory Appl.* **2016**, *10*, 1904–1915. [[CrossRef](#)]
26. Cui, P.; Li, S.; Zhao, G.; Peng, C. Suppression of harmonic current in active-passive magnetically suspended CMG using improved repetitive controller. *IEEE/ASME Trans. Mechatron.* **2016**, *21*, 2132–2141. [[CrossRef](#)]
27. Zheng, T.; Xu, X.; Lu, X.; Hao, L.; Xu, F. Learning adaptive sliding mode control for repetitive motion tasks in maglev rotary table. *IEEE Trans. Ind. Electron.* **2022**, *69*, 1836–1846. [[CrossRef](#)]
28. Ma, L.; Bazzoli, P.; Sammons, P.M.; Landers, R.G.; Bristow, D.A. Modeling and calibration of high-order joint-dependent kinematic errors for industrial robots. *Robot. Comput.-Integr. Manuf.* **2018**, *50*, 153–167. [[CrossRef](#)]
29. Li, X.; Song, C.; Yang, Y.; Zhu, C.; Liao, D. Optimal design of wave generator profile for harmonic gear drive using support function. *Mech. Mach. Theory* **2020**, *152*, 103941. [[CrossRef](#)]
30. Ramos, G.A.; Ruget, R.I.; Costa-Castello, R. Robust repetitive control of power inverters for standalone operation in DG systems. *IEEE Trans. Energy Convers.* **2020**, *35*, 237–247. [[CrossRef](#)]
31. Wu, X.H.; Panda, S.K.; Xu, J.X. Design of a plug-in repetitive control scheme for eliminating supply-side current harmonics of three-phase PWM boost rectifiers under generalized supply voltage conditions. *IEEE Trans. Power Electron.* **2010**, *25*, 1800–1810. [[CrossRef](#)]
32. Zhang, M.; Huang, L.; Yao, W.; Lu, Z. Circulating harmonic current elimination of a CPS-PWM-based modular multilevel converter with a plug-in repetitive controller. *IEEE Trans. Power Electron.* **2014**, *29*, 2083–2097. [[CrossRef](#)]
33. Djouda, B.S.; Moukam Kakmeni, F.M.; Guemkam Ghomsi, P.; Ndjomatchoua, F.T.; Tchawoua, C.; Tonnang, H.E.Z. Theoretical analysis of spatial nonhomogeneous patterns of entomopathogenic fungi growth on insect pest. *Chaos Interdiscip. J. Nonlinear Sci.* **2019**, *29*, 053134. [[CrossRef](#)]
34. Tsai, M.C.; Yao, W.S. Design of a plug-in type repetitive controller for periodic inputs. *IEEE Trans. Control Syst. Technol.* **2002**, *10*, 547–555. [[CrossRef](#)]
35. Pipeleers, G.; Demeulenaere, B.; Schutter, J.D.; Swevers, J. Robust high-order repetitive control: Optimal performance trade-offs. *Automatic* **2008**, *44*, 2628–2634. [[CrossRef](#)]
36. Wu, B.; Bodson, M. Direct adaptive cancellation of periodic disturbances for multivariable plants. *IEEE Trans. Speech Audi Process.* **2003**, *11*, 538–548.
37. Nakano, M.; She, J.H.; Mastuo, Y.; Hino, T. Elimination of position-dependent disturbances in constant-speed-rotation control systems. *Control Eng. Prac.* **1996**, *4*, 1241–1248. [[CrossRef](#)]
38. Han, B.; Chen, Y.; Li, H.; Yang, L. Discrete model reference adaptive control for gimbal servo system of control moment gyro with harmonic drive. *Math. Probl. Eng.* **2013**, *4*, 289–325.
39. Miyazaki, T.; Ohishi, K. Robust speed control system considering vibration suppression caused by angular transmission error of planetary gear. *IEEE/ASME Trans. Mechatron.* **2002**, *7*, 235–244. [[CrossRef](#)]
40. Şahin, M.E.; İbrahim Okumuş, H.; Aydemir, M.T. Implementation of an electrolysis system with DC/DC synchronous buck converter. *Int. J. Hydrog. Energy* **2014**, *39*, 6802–6812. [[CrossRef](#)]
41. Somkun, S.; Sirisamphanwong, C.; Sukchai, S. A DSP-based interleaved boost DC–DC converter for fuel cell applications. *Int. J. Hydrog. Energy* **2015**, *40*, 6391–6404. [[CrossRef](#)]
42. Aden, I.A.; Kahveci, H.; Şahin, M.E. Design and implementation of single-input multiple-output DC–DC buck converter for electric vehicles. *J. Circuits. Syst. Comput.* **2021**, *30*, 2150228. [[CrossRef](#)]

43. Bower, P.; Dedic, I. High speed converters and DSP for 100G and beyond. *Opt. Fiber Technol.* **2011**, *17*, 464–471. [[CrossRef](#)]
44. Mattavelli, P.; Tubiana, L.; Zigliotto, M. Torque-ripple reduction in PM synchronous motor drives using repetitive current control. *IEEE Trans. Power Electron.* **2005**, *20*, 1423–1431. [[CrossRef](#)]
45. Shan, Y.; Leang, K.K. Dual-stage repetitive control with prandtl-ishlinskii hysteresis inversion for piezo-based nanopositioning. *Mechatronics* **2012**, *22*, 271–281. [[CrossRef](#)]
46. Cui, P.; Wang, Q.; Li, S.; Gao, Q. Combined FIR and fractional-order repetitive control for harmonic current suppression of magnetically suspended rotor system. *IEEE Trans. Ind. Electron.* **2017**, *64*, 4828–4835. [[CrossRef](#)]
47. Cui, P.; Wang, Q.; Zhang, G.; Gao, Q. Hybrid fractional repetitive control for magnetically suspended rotor systems. *IEEE Trans. Ind. Electron.* **2018**, *65*, 3491–3498. [[CrossRef](#)]